Article

Large recoverable elastic energy in chiral metamaterials via twist buckling

https://doi.org/10.1038/s41586-025-08658-z

Received: 7 March 2024

Accepted: 16 January 2025

Published online: 12 March 2025

Open access

Check for updates

Xin Fang[1]✉, Dianlong Yu[1], Jihong Wen[1], Yifan Dai[1], Matthew R. Begley[2], Huajian Gao[3] & Peter Gumbsch[4,5]✉

Mechanical metamaterials with high recoverable elastic energy density, which we refer to as high-enthalpy elastic metamaterials, can offer many enhanced properties, including efficient mechanical energy storage[1,2], load-bearing capability, impact resistance and motion agility. These qualities make them ideal for lightweight, miniaturized and multi-functional structures[3–8]. However, achieving high enthalpy is challenging, as it requires combining conflicting properties: high stiffness, high strength and large recoverable strain[9–11]. Here, to address this challenge, we construct high-enthalpy elastic metamaterials from freely rotatable chiral metacells. Compared with existing non-chiral lattices, the non-optimized chiral metamaterials simultaneously maintain high stiffness, sustain larger recoverable strain, offer a wider buckling plateau, improve the buckling strength by 5–10 times, enhance enthalpy by 2–160 times and increase energy per mass by 2–32 times. These improvements arise from torsional buckling deformation that is triggered by chirality and is absent in conventional metamaterials. This deformation mode stores considerable additional energy while having a minimal impact on peak stresses that define material failure. Our findings identify a mechanism and provide insight into the design of metamaterials and structures with high mechanical energy storage capacity, a fundamental and general problem of broad engineering interest.

Materials with high recoverable elastic energy density (that is, enthalpy ϕ) are in demand for many applications, but this requires a combination of high modulus (E_s), high strength and large recoverable strain (ε_{limit})[12,13]. Carbon nanotubes reach extremes at the nanoscale[14,15], yet achieving high enthalpy at the macroscale remains challenging[16,17]. Metamaterials[18–21] can offer extraordinary stiffness, shape control[22,23] and wave manipulation[24,25] by tailoring their topologies and deformation modes[18,26], including elastic buckling[27,28]. A higher-yet-wider buckling plateau on load-deformation curves is desirable for greater energy storage (Fig. 1h). However, in existing designs (Fig. 1c–e), achieving large recoverable strain is accompanied by a reduction of plateau stress, even for tensegrity lattices[29]. This limitation arises from bending-dominated buckling modes, which limits macroscopic stresses while generating large local strains that drive failure. Here we propose an approach to circumvent this limitation and improve recoverable enthalpy: chiral structures that incorporate twisting, compression and bending.

Buckling of chiral and non-chiral rods

Elastic energy in conventional rod-based lattices (Fig. 1c–e) is stored in rods that generally exhibit the first buckling mode when compressed (Fig. 1b and Methods). We use analytical modelling and nonlinear finite element analyses (FEAs) to explain the scaling of energy storage during buckling, which are then extended to include torsion[30] (Methods and Supplementary Notes).

To begin, consider a doubly clamped rod of radius r, length L_0 and Young's modulus E_s subjected to a vertical compression force (F_{1rod}) or axial displacement (Δ): the rod responds initially in pure compression followed by bending buckling (Supplementary Video 1). This individually induces maximal von Mises stress $\sigma_v = \sigma_{cpr}$ and $\sigma_v = \sigma_{cpr} + \sigma_{bend}$ on the outer surface, with σ_{cpr} from compression and σ_{bend} from bending. Failure is assumed to be controlled by σ_v. The analytical model shows that a buckled rod stores strain energy

$$U_{1rod} = U_{bend} + U_{cpr} = \frac{\pi r^2 (L_0 - \Delta)\sigma_{bend}^2}{16E_s} + \frac{\pi r^2 L_0 \sigma_{cpr}^2}{2E_s}. \quad (1)$$

F_{1rod} and U_{1rod} are normalized by $F_s = E_s \pi r^2/4L_0^2$ and $U_s = \pi r^2 L_0 E_s/1{,}000$, respectively.

Straight rods undergo sudden buckling, whereas small imperfections smoothen the buckling process[30] with a slightly reduced plateau load, max(F_{1rod}) (Fig. 2a and Extended Data Fig. 2a,b). Unless otherwise stated, we use rods with moderate slenderness ratio of $2r/L_0 = 0.1$ and $r = 1.5$ mm for comparison. Properties of thick rods are provided in Extended Data Figs. 3 and 6.

Lattices consisting of angled rods (Fig. 1c–e) show improved stiffness and max(F_{1rod}) with increased oblique angle (θ) (Fig. 2a). However,

[1]National Key Laboratory of Equipment State Sensing and Smart Support, College of Intelligent Science and Technology, National University of Defense Technology, Changsha, China. [2]Department of Mechanical Engineering, University of California, Santa Barbara, Santa Barbara, CA, USA. [3]Mechanics-X Institute, Tsinghua University, Beijing, China. [4]Institute for Applied Materials, Karlsruhe Institute of Technology, Karlsruhe, Germany. [5]Fraunhofer Institute for Mechanics of Materials IWM, Freiburg, Germany. ✉e-mail: xinfangdr@sina.com; peter.gumbsch@kit.edu

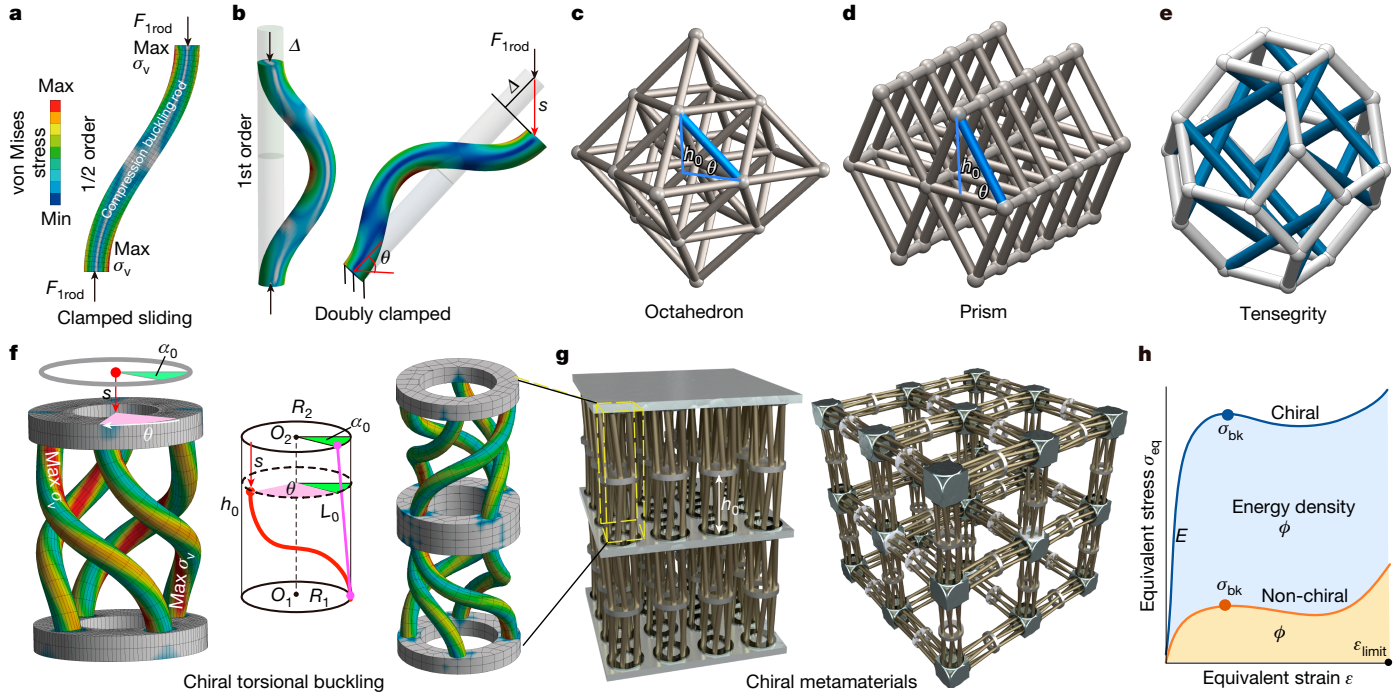

Fig. 1 | Deformation of chiral and non-chiral metamaterials. a, A 1/2-order lateral bending buckling of clamped-sliding rods under compression force F_{1rod}, observed in chiral metamaterials in **f**. **b**, A first-order buckling mode of doubly clamped vertical and oblique rods in non-chiral lattices. The colour bars in **a**, **b** and **f** show the distribution of Mises stress σ_v. **c**–**e**, Octahedron (**c**), prism (**d**) and tensegrity (**e**) lattices. **f**, Compression-twist buckling of chiral metacells. The cente schematic shows a purple straight chiral arm buckling into a red curved arm with a global twisting angle (θ). **g**, Multilayered and 3D chiral metamaterials consisting of decoupled metacells. **h**, Schematic showing the enhanced energy density (ϕ), load-bearing strength (σ_{bk}) and high stiffness (E) of chiral metamaterials.

in buckled rods, $\sigma_{cpr} \ll \sigma_{bend}$, resulting in nearly constant energy $U_{1rod} \approx \pi r^2 L_0 \sigma_v^2 / 16 E_s$ for a given stress σ_v, regardless of the angle θ (Fig. 2b). Moreover, U_{bend} in equation (1) is independent of buckling order (n). Thus, adjusting the oblique angle or inducing high-order buckling modes ($n > 1$) can change max(F_{1rod}) but cannot effectively improve U_{1rod} for a specified material strength (σ_v). This severely limits energy storage in strut-based metamaterials.

To overcome this limitation, we must introduce additional deformation modes beyond bending and compression. Chiral metamaterials[31–33], with coupling between axial deformation and twisting, offer exciting possibilities to store more energy by torsion. The potential of these structures is defined by their post-buckling behaviour and its implications on force, stress and energy[34–36]. We propose chiral metamaterials with independent and rotatable cylindrical metacells (Fig. 1g) that are distinct from previous chiral structures[37–39]. They exhibit high-energy buckling modes that improve enthalpy (ϕ) and plateau strength (σ_{bk}) for fixed material strength (Fig. 1h).

Here we consider a mirror-symmetric metacell (Fig. 1f and Extended Data Fig. 1), in which every half-cell incorporates two coaxial tori (O_1, O_2) with radii R_1 and R_2 at a distance h_0. N oblique rods, serving as chiral arms, are periodically fixed to the tori. At rest, the two tori are relatively rotated by an angle α_0. When fixing torus O_1 and vertically compressing torus O_2 by s, a relative rotation angle θ ensues between them (Supplementary Video 2). The global strain $\varepsilon = s/h_0$ is used throughout. Chiral buckling causes the twisted rod to bulge outwards and forms a helix under large compression (Fig. 1f). We define this mode as twist buckling.

We established an analytical model (Methods) that fully captures post-buckling behaviours of chiral rods (Fig. 2c,e and Extended Data Fig. 4). This model illustrates that chiral twist buckling involves four deformation modes in each rod: in-plane bending, out-of-plane bending, twisting and compression (Extended Data Fig. 1). The stored elastic energy can be written as

$$U_{1rod} = E_s \pi r^4 \left[\frac{\pi^4 a_{in}^2}{L_x^3} + \frac{\pi^4 a_{out}^2}{L_0^3} + \frac{\theta^2}{8(1+\upsilon)L_0} + \frac{\Delta_{cpr}^2}{2L_0 r^2} \right], \quad (2)$$

where $2a_{in}$, $2a_{out}$ and Δ_{cpr} are the maximal amplitudes of in-plane, out-of-plane and compression deformation modes, respectively; υ is Poisson's ratio; and L_x is the length of the twisted rod.

Both in-plane and out-of-plane bending follow the 1/2-order buckling mode with clamped-sliding ends (Fig. 1a). Out-of-plane bending couples with global twisting between the two tori, introducing two more energy sources related to a_{out} and angle θ that are absent in non-chiral structures in equation (1). Chiral metamaterials show high stiffness at small strain $\varepsilon < 0.02$, at which the rods and torus are twisted equally by θ. They buckle smoothly with increasing load instead of abruptly as with purely bending buckling. Increasing α_0 gives a smoother force-deformation curve (Fig. 2c). For unequal torus radii ($R_1 \neq R_2$), both plateau load max(F_{1rod}) and energy (U_{1rod}) are lower than the case of equal radii (Extended Data Fig. 3a–c). We consider $R = R_1 = R_2$ in the following. For specified ε, reducing α_0 or R enhances max(F_{1rod}) and U_{1rod}, with R having greater effects (Fig. 2f and Extended Data Fig. 5). Performance evaluation is based on the limitation of maximal von Mises stress (σ_v) in chiral rods, which occurs in the twisted ribbon region on the rod surface (Fig. 1f).

In prismatic or octahedron lattices, rods with angles $\theta > 45°$ may not buckle within $\sigma_v < 0.1E_s$ (Fig. 2a). Here, the same chiral rod with $R = 6$ mm and $\alpha_0 = 5°$ gives max(F_{1rod}/F_s) = 0.8 (Fig. 2c), surpassing that of a non-chiral rod with $\theta = 40°$ by 30%. The global limit strain ε_{limit} for $\sigma_v = 0.1E_s$ also increases from 0.076 to 0.1, providing a broader safe plateau for storing more energy.

The stress–energy plot of the moderate slenderness rod (Fig. 2e) shows the superior energy storage of chiral buckling compared with bending buckling for specific strength σ_v. Different chiral models show convergent stress–energy curves, indicating robust performance.

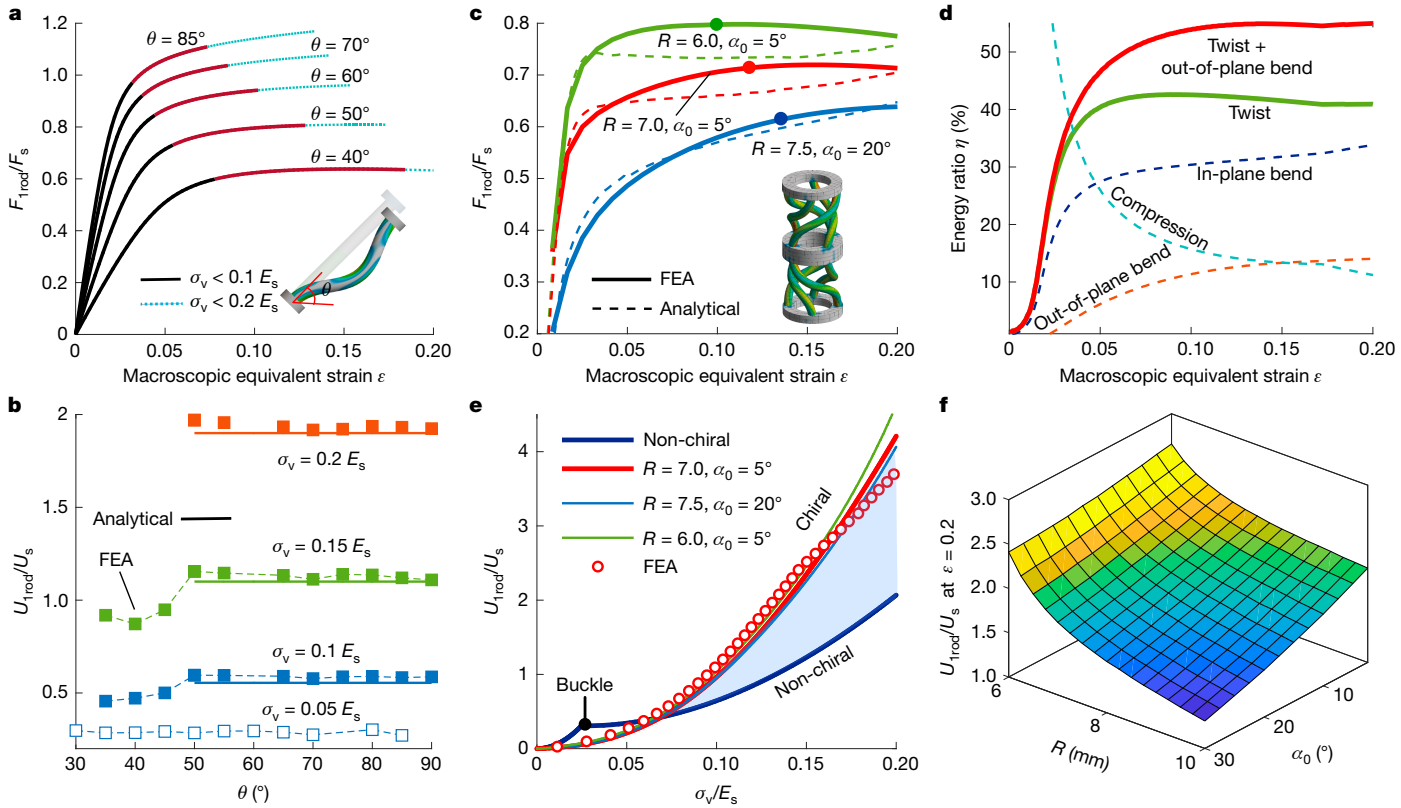

Fig. 2 | Buckling of chiral and non-chiral rods. a,**b**, Angled non-chiral rods. **c**–**f**, Chiral rods. **a**, Normalized force (F_{1rod}/F_s) versus macroscopic strain ($\varepsilon = s/L_0 \sin\theta$) of angled rods with oblique angle θ. Micro-bending imperfection is included here. **b**, Normalized energy (U_{1rod}/U_s) under different maximal von Mises stresses (σ_v) versus θ of perfectly straight rods. **c**, Theoretical force–strain curves of typical chiral models. Filled circles are points for $\sigma_v = 0.1E_s$. None of the curves reach $\sigma_v = 0.2E_s$ at $\varepsilon = 0.2$. **d**, Proportions of energy from different deformation modes. **e**, Energy–stress plot of straight rods with $2r/L_0 = 0.1$ (U_{1rod}/U_s versus σ_v/E_s). Discrete points are FEA results for $R = 7$ mm. **f**, Influence of initial angle (α_0) and radius (R) on U_{1rod}/U_s at $\varepsilon = 0.2$.

As non-chiral rods store energy by pure compression before buckling, they can store slightly more energy than chiral rods near the buckling point if imperfections can be avoided (Extended Data Fig. 2b). However, beyond that point, chiral rods store more energy. Larger deformation or allowable stress further enhances this advantage. For $\sigma_v = 0.2E_s$, a chiral rod stores twice the energy of a non-chiral rod.

This advantage is greater in thinner rods because of their low buckling thresholds (Extended Data Fig. 3d). Metamaterials consisting of thick rods may favour non-chiral designs if suitable constraints ensure the ideal first buckling. Otherwise, their rods generally follow the 1/2-order lateral buckling mode, which has only 1/16 of the critical energy compared with the first mode (Methods). In this case, chiral rods still store about two to four times higher energy (Extended Data Fig. 6).

Mechanism analysis

We can map the twist buckling of freely rotatable chiral metacell into the micropolar elasticity framework[40–42] (Supplementary Fig. 8). It suggests that chirality, defined as the coupling of compression and global torsion, dominates the properties under large compression (Supplementary Note 4). This is confirmed by the energy proportions (η) of the four deformation modes predicted by the chiral twist buckling theory (Fig. 2d). Axial compression dominates for $\varepsilon < 0.02$, but as deformation increases, contributions from in-plane bending and in-rod twisting rise. At $\varepsilon > 0.05$, the in-rod twisting accounts for 40% energy, as confirmed by phased loading FEA in Extended Data Fig. 7. In-rod twisting together with out-of-plane bending—the two modes absent in non-chiral lattices—can contribute 55% energy. Therefore, the enhanced performance of chiral rods is attributed to invoking torsion.

Furthermore, chiral rods have a favourable stress distribution. Although bending causes maximal stresses at the rod ends in confined sections (Fig. 1a), the in-plane and out-of-plane bending modes are orthogonal and do not compound stress. The maximal normal stress is given by $\sigma_{norm} = \sigma_{in} + \sigma_{cpr}$, with in-plane being the dominant contributor. Torsion induces nearly uniform shear stress (τ) perpendicular to σ_{norm} across the entire rod surface. Thus, the maximal von Mises stress becomes

$$\sigma_v = \sqrt{(\sigma_{in} + \sigma_{cpr})^2 + 3\tau^2}. \quad (3)$$

As $\tau \ll \sigma_{in}$, invoking torsion adds stored energy while only marginally raising σ_v (Fig. 2e and Methods). Reducing α_0 or R increases F_{1rod}, U_{1rod} and the contribution from twisting (Extended Data Fig. 5).

Performance comparison

Beyond a single rod, the entire chiral metamaterial shows greater improvement for specified volume (Methods). We compare the performance of chiral metamaterials to extensive non-chiral models using FEA and analytical methods (Fig. 3a,f). They consist of identical rods unless otherwise specified. In theory, half a chiral metacell can tightly pack $\pi R/r$ rods around its torus. Here the internal core remains vacant and we only take half the number, $N = \pi R/2r$, ensuring ample space to avoid contact between arms. By contrast, parallel rods in the prism lattice are densely arranged with a distance of $4r$. All metamaterials are characterized by macroscopic properties: load-bearing strength σ_{bk} (Fig. 1h), limit deformability ε_{limit} at rod strength, modulus E, energy density (enthalpy) ϕ and mass density ρ. They are normalized

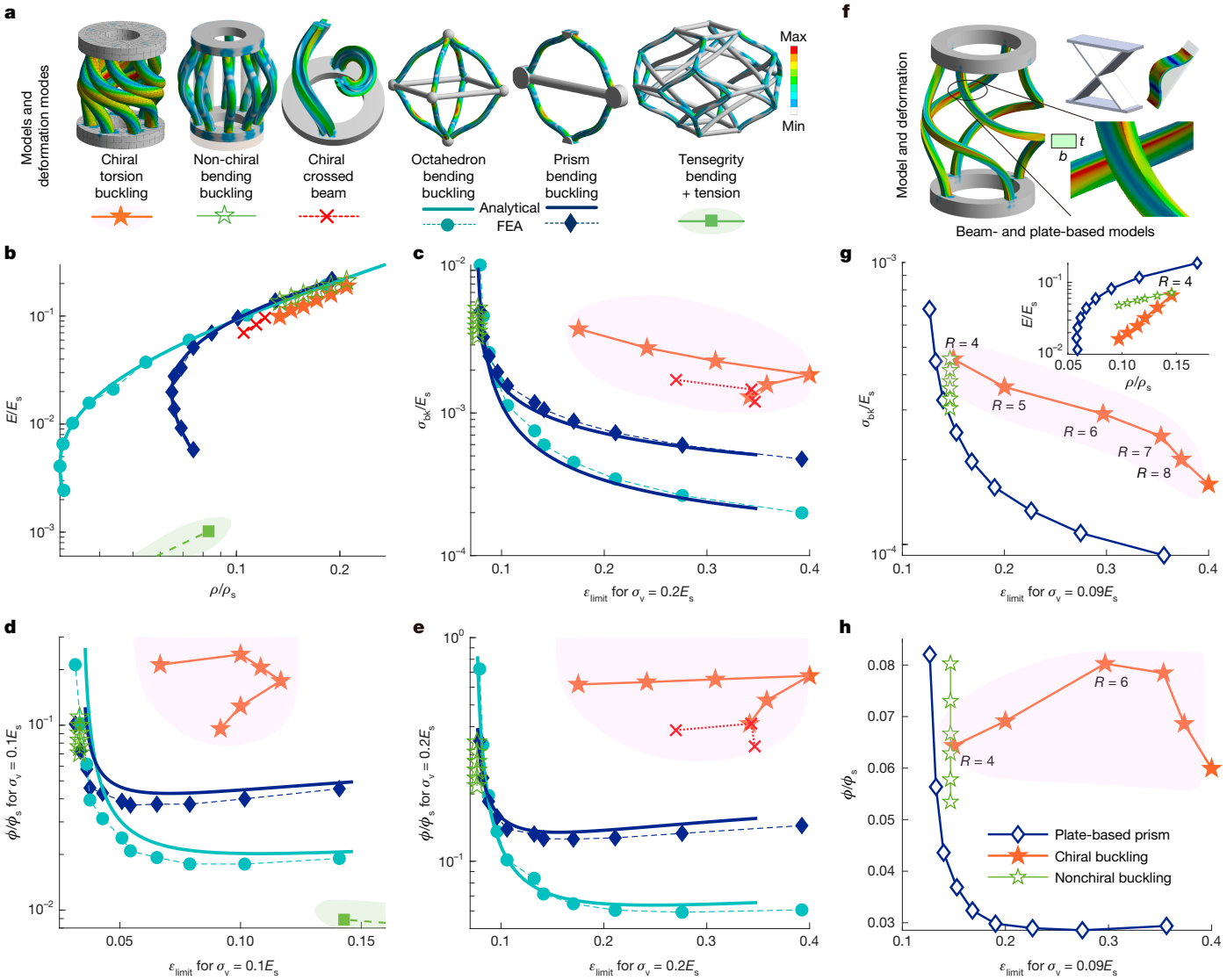

Fig. 3 | Metamaterial performances. ε_{limit} denotes the global strain at material strength (σ_v). Performances of octahedron and prism lattices are controlled by the oblique angle (θ) of the rod, whose ε_{limit} increases as θ decreases. For chiral metamaterials, $h_0 = 30$ mm and radius (R) is variable. **a**–**e**, Rod-based metamaterials. **a**, Legend and deformation modes for metamaterial configurations in **b**–**e**. **b**, Ashby map of E/E_s versus ρ/ρ_s. **c**, Bearing strength $\sigma_{bk} = \max(\sigma_{eq})$ on the buckling plateau versus ε_{limit} for $\sigma_v = 0.2E_s$. **d**, Enthalpy (ϕ/ϕ_s) versus ε_{limit} for $\sigma_v = 0.1E_s$. **e**, ϕ/ϕ_s - ε_{limit} for $\sigma_v = 0.2E_s$. **f**–**h**, Plate- and beam-based metamaterials, in which the plate and square beam have the thickness $t = 1$ and length $L_0 = 30$ mm. Max(σ_v) occurs at the corner edge of the twisted beam. **f**, Legend and deformation modes for configurations in **g** and **h**. **g**,**h**, σ_{bk} (**g**) and ϕ/ϕ_s (**h**) versus ε_{limit} for $\sigma_v = 0.09E_s$. Inset in **g**: an E–ρ map.

by the modulus (E_s), enthalpy ($\phi_s = E_s/1{,}000$) or density (ρ_s) of rods (Methods).

Bend-dominated tetradecahedron (Kelvin) trusses possess low stiffness and enthalpy, which can be improved by tensegrity design[29]. However, despite withstanding higher ε_{limit}, the tensegrity trusses—even with doubled rod thickness—exhibit 50× lower modulus and 5× lower enthalpy than the octahedron lattice of equal density (Fig. 3b,d and Extended Data Fig. 8). In octahedron and prism lattices, all oblique rods are ideally assumed to follow the first buckling mode (Fig. 3a); reducing the oblique angle (θ) of the rod increases the recoverable strain ε_{limit} (Fig. 2a) but affects the density (ρ/ρ_s) non-monotonously. Their stiffness and density follow the proportional law $E/E_s \sim (\rho/\rho_s)^1$ (where ~ means 'distributed as') for $\theta > 60°$ (Fig. 3b), in which the response is stretch-dominated[18,43]. Plotting σ_{bk}/E_s and ϕ/ϕ_s against ε_{limit} shows that these non-chiral lattices follow the undesirable trade-off laws between bearing strength σ_{bk} (or enthalpy ϕ) and ε_{limit} (Fig. 3c–e). Although prism lattices outperform octahedron lattices in σ_{bk} and ϕ owing to larger ρ/ρ_s, their σ_{bk} and ϕ are low and nearly constant beyond a small ε_{limit}.

Analytical studies show that reducing α_0 or R increases chiral metamaterial E, σ_{bk} and ϕ (Extended Data Fig. 5). We verified this through simulations with R ranging from 5 mm to 10 mm ($N = 5$–10) for a specified height $h_0 = 30$ mm. A moderate dimension around $R = 8$ mm offers the largest ε_{limit}. The stiffness (E/E_s) is comparable with high-density non-chiral lattices (Fig. 3b). Notably, chiral metamaterial maintains 5–10 times higher σ_{bk} and 5–20 times higher enthalpy than the prism and octahedron lattices. The chiral metamaterial surpasses the tensegrity trusses with more than 100× enthalpy. Greater improvement is observed at higher material strengths ($\sigma_v = 0.2E_s$), but even metals with limited strength show improved performance in the experiments below.

If we made chiral metacells non-rotatable under compression to show the first bending in rods (Fig. 3a–e), the properties would be similar to other stretch-dominated lattices composed of nearly vertical rods:

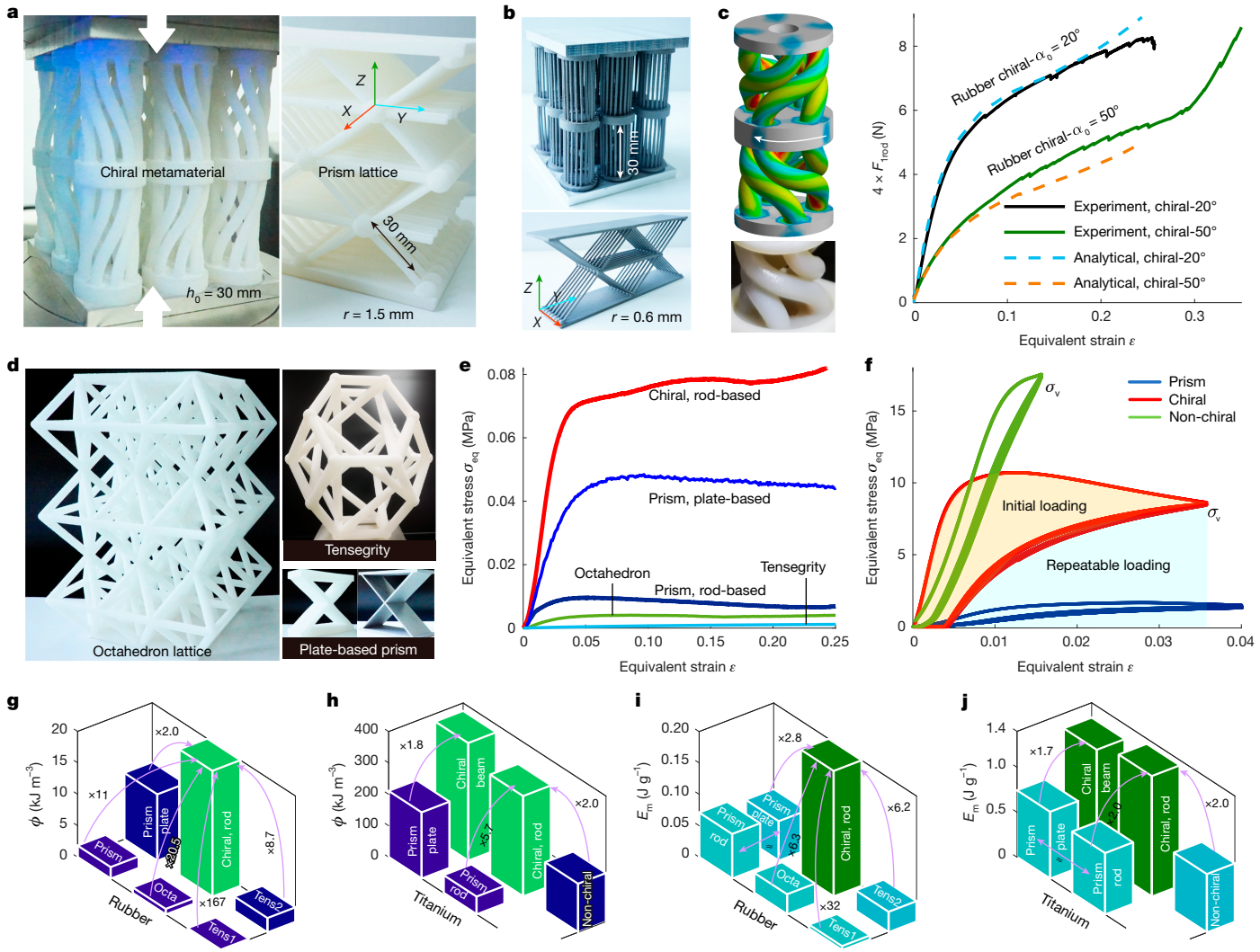

Fig. 4 | Experimental results. a–d, Three-dimensional printed samples. **a**, Chiral twist buckling of a 3 × 3 metamaterial under compression. **b**, Pictures of typical titanium-alloy samples. Top: chiral metamaterial. Bottom: the prism lattice. **c**, Force–strain curves and deformation of typical rubber chiral metacells. In the chiral-50° sample, the neighbouring rods contact for $\varepsilon > 0.3$. **d**, Octahedron, tensegrity tetradecahedron and prism lattices composed of rods or plates. **e**,**f**, Equivalent stress–strain curves of rubber samples (**e**) and rod-based titanium-alloy samples (**f**), with shaded areas representing the range for calculating enthalpy ϕ and energy ratio E_m = energy/mass. In **f**, the shaded areas are distinguished into the initial and repeatable loading processes; and 'non-chiral' denotes the non-rotatable chiral unit that exhibits bending, reaching equal in-rod stress σ_v with the chiral model. **g**–**j**, ϕ (**g**,**h**) and E_m (**i**,**j**) of rod-, plate- and beam-based metamaterials made of rubber (**g**,**i**) or titanium (**h**,**j**). For titanium samples, the results from the initial loading process are used. Here, octa and tens represent octahedron and tensegrity lattices, respectively; the rod radius is r = 1.5 mm for tens1 and r = 3 mm for tens2.

achieving high E, σ_{bk} and ϕ but at the cost of small ε_{limit}. Disregarding ε_{limit}, chiral buckling entails about two to three times greater enthalpy than non-chiral mode. This directly reflects the additional contributions from in-rod twisting and out-of-plane bending.

Straight rectangle-sectioned beam fails to support large chiral buckling, as they preferentially bend along the thinnest axis (Supplementary Video 3). Although chiral units based on X-sectioned beams can display large twist buckling, they underperform the units comprising same-size round rods (Fig. 3 and Supplementary Video 2). We further compare chiral models comprising N square beams to the prism lattices comprising plates with the same thickness t (Fig. 3f–h). Here, t = 1, $R \approx 4$–9 mm and $N = 2\pi R/1.2t$. The prism lattice follows identical trade-off laws in Fig. 3b–e. Despite having lower E/E_s under equal density (ρ/ρ_s), chiral configurations provide 2.8 times higher σ_{bk} and ϕ at large strains.

All these findings indicate that chiral metamaterials outperform non-chiral lattices in maintaining high stiffness and offering superior load-bearing capacity and enthalpy at large limit strain.

Experiments

For experimental demonstration, we fabricated various rod-, beam- and plate-based specimens using three-dimensional printing, using rubber and TC4 titanium alloy. Layered chiral metamaterials were assembled from separated units (Fig. 4a,b). These chiral, prism, octahedron, Kelvin and tensegrity specimens were designed following the guidance in Fig. 3e,h, ensuring their primitives exhibit approximate von Mises stress (σ_v) at specified global strain levels (Methods). Their compression buckling behaviours were tested (Extended Data Figs. 9 and 10 and Supplementary Videos 4–7). The chiral twist buckling behaviours closely align with analytical predictions (Fig. 4a,c). The performance indicators of all specimens are summarized in Extended Data Table 1, with the main results presented in Fig. 4g–j, showing the improvements from non-chiral to chiral metamaterials consisting of primitives with the same dimensions (plate thickness = rod diameter = $2r$ = 3 mm).

Rubber samples can sustain repeatable deformation until the rods make contact. For rod-based architectures, the chiral metamaterial

obtains 7.5× higher buckling strength σ_{bk} over the high-stiffness prism lattice (Fig. 4e), and achieves 11×, 20×, 167× and 10^5× higher enthalpy compared with prism, octahedron, tensegrity and Kelvin lattices, respectively (Fig. 4g). It even exceeds the tensegrity lattice with doubled rod thickness ($2r$ = 6 mm) by 8.7×, and exceeds the plate-based prism lattice with 1.8× density (ρ) by two times. These improvements align with the simulations in Fig. 3.

For TC4 samples (Fig. 4b,f), the initial loading follows the theoretical buckling process. On unloading, a plastic strain and augmented angle α_0 persist. Subsequent cycles remain repeatable within the macroscopic strain amplitude, preserving relative performance. Despite the limited deformability, the metal chiral architecture enhances σ_{bk} by 5.7× over prism lattice and even obtains 1.8–2× higher enthalpy than the plate-based prism, which is 3.5× denser (Fig. 4h). For chiral metamaterials, the non-rotatable mode shows higher stiffness but lower limit strain (Fig. 4f), whereas twist buckling stores twice as much energy.

With a focus on mass instead of volume, we evaluate E_m = energy/m_{rod}, where m_{rod} is the total mass of buckling rods. The plate- and rod-based prism lattices have approximately the same E_m (Fig. 4i,j), indicating comparable energy ratios for same-size primitives. At ε = 0.25, the rubber chiral metamaterial obtains 2.8×, 6.3× and 6.2–32× higher E_m than the prism, octahedron and tensegrity lattices, respectively (Fig. 4i). The titanium chiral metamaterial surpasses all non-chiral lattices in E_m by about 2× (Fig. 4j), validating the improvements from rod twisting (Fig. 2e).

Performance decreases from the ideal case when a lattice exhibits global lateral buckling (as in the prism lattices in Supplementary Video 5) or nonuniform buckling (as in the octahedron lattice in Supplementary Video 6). Although our chiral metamaterials are assembled with decoupled units, they reliably exhibit the desired torsional buckling without external constraints (Fig. 4a and Supplementary Video 4).

Conclusions

Here we propose a strategy to create metamaterials with high enthalpy by invoking torsion, alongside bending and compression, within chiral metacells, forming the unique chiral twist buckling. Compared with various existing non-chiral lattices, the non-optimized chiral metamaterials maintain high stiffness and achieve larger recoverable deformation, 5–10× buckling strength, 2–160× enthalpy and 2–32× energy per mass within the limit of material strength. The performance can be further enhanced by using a denser arrangement of chiral arms. High-enthalpy metamaterials have potential applications in lightweight and miniaturized design, elastic energy storage[44], impact protection[45,46], torsional modulation and actuation. The twist buckling plateau also offers low-dynamic stiffness under heavy load, opening possibilities for low-frequency vibration isolators[47].

Online content

Any methods, additional references, Nature Portfolio reporting summaries, source data, extended data, supplementary information, acknowledgements, peer review information; details of author contributions and competing interests; and statements of data and code availability are available at https://doi.org/10.1038/s41586-025-08658-z.

1. Koohi-Fayegh, S. & Rosen, M. A. A review of energy storage types, applications and recent developments. *J. Energy Storage* **27**, 101047 (2020).
2. Amirante, R., Cassone, E., Distaso, E. & Tamburrano, P. Overview on recent developments in energy storage: mechanical, electrochemical and hydrogen technologies. *Energy Convers. Manage.* **132**, 372–387 (2017).
3. Alexander, R. M. & Bennet-Clark, H. C. Storage of elastic strain energy in muscle and other tissues. *Nature* **265**, 114–117 (1977).
4. Zhan, H., Dong, B., Zhang, G., Lu, C. & Gu, Y. Nanoscale diamane spiral spring for high mechanical energy storage. *Small* **18**, e2203887 (2022).
5. Hawkes, E. W. et al. Engineered jumpers overcome biological limits via work multiplication. *Nature* **604**, 657–661 (2022).
6. Liu, B., Ge, W., Zhao, D., Zou, Z. & Li, B. Mechanical design and energy storage efficiency research of a variable stiffness elastic actuator. *Int. J. Adv. Robot. Syst.* https://doi.org/10.1177/1729881420930950 (2020).
7. Scarfogliero, U., Stefanini, C. & Dario, P. The use of compliant joints and elastic energy storage in bio-inspired legged robots. *Mech. Mach. Theory* **44**, 580–590 (2009).
8. Gopalakrishnan, S. & Rajapakse, Y. (eds) *Blast Mitigation Strategies in Marine Composite and Sandwich Structures* (Springer, 2018).
9. Begley, M. R., Gianola, D. S. & Ray, T. R. Bridging functional nanocomposites to robust macroscale devices. *Science* **364**, eaav4299 (2019).
10. Raabe, D., Tasan, C. C. & Olivetti, E. A. Strategies for improving the sustainability of structural metals. *Nature* **575**, 64–74 (2019).
11. Liu, L. et al. Making ultrastrong steel tough by grain-boundary delamination. *Science* **368**, 1347–1352 (2020).
12. Lu, K. The future of metals. *Science* **328**, 319–320 (2010).
13. Li, H. et al. Uniting tensile ductility with ultrahigh strength via composition undulation. *Nature* **604**, 273–279 (2022).
14. Dusoe, K. J. et al. Ultrahigh elastic strain energy storage in metal-oxide-infiltrated patterned hybrid polymer nanocomposites. *Nano Lett.* **17**, 7416–7423 (2017).
15. Bai, Y. et al. Storage of mechanical energy based on carbon nanotubes with high energy density and power density. *Adv. Mater.* **31**, e1800680 (2019).
16. Ali, A., Rahimian Koloor, S. S., Alshehri, A. H. & Arockiarajan, A. Carbon nanotube characteristics and enhancement effects on the mechanical features of polymer-based materials and structures—a review. *J. Mater. Res. Technol.* **24**, 6495–6521 (2023).
17. Ramezani, M., Dehghani, A. & Sherif, M. M. Carbon nanotube reinforced cementitious composites: a comprehensive review. *Constr. Build. Mater.* **315**, 125100 (2022).
18. Zheng, X. et al. Ultralight, ultrastiff mechanical metamaterials. *Science* **344**, 1373–1377 (2014).
19. Fang, X. et al. Programmable gear-based mechanical metamaterials. *Nat. Mater.* **21**, 869–876 (2022).
20. Zhang, X., Zangeneh-Nejad, F., Chen, Z., Lu, M. & Christensen, J. A second wave of topological phenomena in photonics and acoustics. *Nature* **618**, 687–697 (2023).
21. Fang, X., Wen, J., Bonello, B., Yin, J. & Yu, D. Ultra-low and ultra-broad-band nonlinear acoustic metamaterials. *Nat. Commun.* **8**, 1288 (2017).
22. Kim, M. et al. Harnessing a paper-folding mechanism for reconfigurable DNA origami. *Nature* **619**, 78–86 (2023).
23. Chen, T., Pauly, M. & Reis, P. M. A reprogrammable mechanical metamaterial with stable memory. *Nature* **589**, 386–390 (2021).
24. Qi, J. et al. Recent progress in active mechanical metamaterials and construction principles. *Adv. Sci.* **9**, 2102662 (2022).
25. Wenz, F. et al. Designing shape morphing behavior through local programming of mechanical metamaterials. *Adv. Mater.* **33**, 2008617 (2021).
26. Zheng, X. et al. Multiscale metallic metamaterials. *Nat. Mater.* **15**, 1100–1106 (2016).
27. Frenzel, T., Findeisen, C., Kadic, M., Gumbsch, P. & Wegener, M. Tailored buckling microlattices as reusable light-weight shock absorbers. *Adv. Mater.* **28**, 5865–5870 (2016).
28. Findeisen, C., Hohe, J., Kadic, M. & Gumbsch, P. Characteristics of mechanical metamaterials based on buckling elements. *J. Mech. Phys. Solids* **102**, 151–164 (2017).
29. Bauer, J., Kraus, J. A., Crook, C., Rimoli, J. J. & Valdevit, L. Tensegrity metamaterials: toward failure-resistant engineering systems through delocalized deformation. *Adv. Mater.* **33**, 2005647 (2021).
30. Simitses, G. J. & Hodges, D. H. *Fundamentals of Structural Stability* (Elsevier, 2006).
31. Frenzel, T., Kadic, M. & Wegener, M. Three-dimensional mechanical metamaterials with a twist. *Science* **358**, 1072–1074 (2017).
32. Chen, Y., Kadic, M., Guenneau, S. & Wegener, M. Isotropic chiral acoustic phonons in 3D quasicrystalline metamaterials. *Phys. Rev. Lett.* **124**, 235502 (2020).
33. Kadic, M., Milton, G. W., van Hecke, M. & Wegener, M. 3D metamaterials. *Nat. Rev. Phys.* **1**, 198–210 (2019).
34. Patil, V. P., Sandt, J. D., Kolle, M. & Dunkel, J. Topological mechanics of knots and tangles. *Science* **367**, 71–75 (2020).
35. Lin, G. et al. Buckling of lattice columns made from three-dimensional chiral mechanical metamaterials. *Int. J. Mech. Sci.* **194**, 106208 (2021).
36. Majumdar, A. & Raisch, A. Stability of twisted rods, helices and buckling solutions in three dimensions. *Nonlinearity* **27**, 2841–2867 (2014).
37. Frenzel, T., Köpfler, J., Jung, E., Kadic, M. & Wegener, M. Ultrasound experiments on acoustical activity in chiral mechanical metamaterials. *Nat. Commun.* **10**, 3384 (2019).
38. Zhou, S. et al. Chiral assemblies of pinwheel superlattices on substrates. *Nature* **612**, 259–265 (2022).
39. Fernandez-Corbaton, I. et al. New twists of 3D chiral metamaterials. *Adv. Mater* **31**, 1807742 (2019).
40. Eringen, A. C. *Microcontinuum Field Theories. I. Foundations and Solids* (Springer, 1999).
41. Liu, X. N., Huang, G. L. & Hu, G. K. Chiral effect in plane isotropic micropolar elasticity and its application to chiral lattices. *J. Mech. Phys. Solids* **60**, 1907–1921 (2012).
42. Chen, Y., Frenzel, T., Guenneau, S., Kadic, M. & Wegener, M. Mapping acoustical activity in 3D chiral mechanical metamaterials onto micropolar continuum elasticity. *J. Mech. Phys. Solids* **137**, 103877 (2020).
43. Cheung, K. C. & Gershenfeld, N. Reversibly assembled cellular composite materials. *Science* **341**, 1219–1221 (2013).

44. Cheng, H. et al. Mechanical metamaterials made of freestanding quasi-BCC nanolattices of gold and copper with ultra-high energy absorption capacity. *Nat. Commun.* **14**, 1243–1243 (2023).
45. Siddique, S. H., Hazell, P. J., Wang, H., Escobedo, J. P. & Ameri, A. A. H. Lessons from nature: 3D printed bio-inspired porous structures for impact energy absorption—a review. *Addit. Manuf.* **58**, 103051 (2022).
46. Zhang, T. et al. Compressive mechanical behaviors of PPR and NPR chiral compression–twist coupling lattice structures under quasi-static and dynamic loads. *Thin-Walled Struct.* **182**, 110234 (2023).
47. Dalela, S., Balaji, P. S. & Jena, D. P. Design of a metastructure for vibration isolation with quasi-zero-stiffness characteristics using bistable curved beam. *Nonlinear Dyn.* **108**, 1931–1971 (2022).

Methods

Finite element analysis

All FEAs were performed using ANSYS, considering large nonlinear geometrical deformations. Typically, one end is fixed while a displacement boundary condition is applied to the other end, allowing us to obtain the von Mises stress, strain energy and reaction force.

Bending buckling mode

We consider the compressive buckling of a doubly clamped rod. Its bending deflection is assumed to be $w(x) = a(1 - \cos bx)$, $b = 2n\pi/L$, where L is the rod length, n denotes the order of bending buckling and x is the position along the rod (Supplementary Note 1). The maximal deflection is $w_{max} = 2a$. The rod in the chiral metacell bends in the $n = 1/2$ mode. A slender primitive rod in non-chiral lattices typically follows the first-order buckling mode $n = 1$ under suitable constraints, but without stiff constraints, some global buckling mode may lead to $n = 1/2$ for the oblique rods (Extended Data Fig. 9b).

We note that the assumption for deflection, $w(x) = a(1 - \cos bx)$, is valid for moderate deformation $\varepsilon < 0.2$. When a rod is deeply buckled, it exhibits more complex deformation patterns. In FEA, these transformations in the bending deflection are adaptively accounted for through geometrical nonlinearity. This transformation is not considered in the analytical theory, which explains the increasing deviation from FEA results in Fig. 2 for $\varepsilon > 0.2$.

Compression buckling of non-chiral rods

Here we briefly describe the results of our analytical model for the compression buckling of a rod. The complete modelling process and mathematical details are provided in Supplementary Note 1. When an axial compression displacement (Δ) is applied to a doubly clamped rod of radius r, length L_0 and Young's modulus E_s, the axial reaction force is F_{1rod}. At first, the stress σ_{cpr} is induced by pure compression. Buckling occurs at a critical force

$$F_c = n^2\pi^3 E_s r^4/L_0^2,$$

where n denotes the order of buckling mode. The critical axial stress for buckling is

$$\sigma_{cpr}^{critical} = n^2\pi^2 E_s r^3/L_0^2.$$

When $F_{1rod} < F_c$, the rod undergoes uniform strain $\varepsilon = \Delta/L_0$ and stress $\sigma_{cpr} = E_s\varepsilon$, storing energy

$$U_{1rod} = U_{cpr} = \frac{V_s\sigma_{cpr}^2}{2E_s} = \frac{\varepsilon^2 V_s E_s}{2},$$

where $V_s = \pi r^2 L_0$ denotes rod volume. In this case, von Mises stress is $\sigma_v = \sigma_{cpr}$. Moreover, the critical energy for buckling is

$$U_{1rod}^{critical} = \frac{E_s V_s n^4\pi^4 r^6}{2L_0^4} = \frac{E_s n^4\pi^5 r^8}{2L_0^3}.$$

This equation shows that the critical energy is proportional to n^4. If the buckling order changes from $n = 1$ to 1/2, the critical energy greatly reduces to 1/16.

When buckling occurs, the stress induced by pure compression (σ_{cpr}) remains nearly constant. In the general case with $n = 1$, bending induces maximal tensile or compressive stresses on the surface near the clamped ends

$$\sigma_{bend} = \frac{4E_s\pi^2 ra}{2(L_0 - \Delta)^2},$$

where $2a$ denotes the bending deflection. Consequently, maximal von Mises stress $\sigma_v = \sigma_{bend} + \sigma_{cpr}$ is found there. In this case, the strain energy stored in a compressive buckling rod is

$$U_{1rod} = U_{bend} + U_{cpr} = \frac{\pi r^2(L_0 - \Delta)\sigma_{bend}^2}{16E_s} + \frac{\pi r^2 L_0\sigma_{cpr}^2}{2E_s}.$$

This equation indicates that σ_{cpr} gets an eight times higher increment ratio of energy than σ_{bend} when increasing stress. Thus, for a specified moderate stress, such as $\sigma_v = 0.1E_s$, a thicker rod obtains higher U_{1rod}/U_s until buckling disappears at this stress level. This equation also indicates that combining bending and compression increases the increment ratio of U_{1rod}/U_s as strain $\varepsilon = \Delta/h_0$ increases.

We note that when analysing the angled rod and chiral rod, the vertical compression displacement is defined as s. In the above equations, Δ denotes the axial compression displacement. $\Delta = s$ for a vertical rod with angle $\theta = 90°$.

Parameter generalization

Based on the theory above, we adopt $F_s = E_s I/L_0^2$ to normalize the compressive force. Moreover, specifying $\xi = \sigma_{cpr}/\sigma_{bend}$, the energy inside a buckled rod can be simplified as

$$U_{1rod} \approx \frac{V_s\sigma_v^2(1 + 8\xi^2)}{16E_s(1 + \xi)^2} = V_s E_s f, \quad f = \frac{\lambda^2(1 + 8\xi^2)}{16(1 + \xi)^2}.$$

Here, $V_s = \pi r^2 L_0$ is the rod volume and $\lambda = \sigma_v/E_s$ is the normalized strength. Then, the enthalpy of a single rod is

$$\phi_{rod} = U_{1rod}/V_s \approx E_s f.$$

The factor f can be approximated as $f \approx 2.5/1{,}000$ for $\xi \to 0$ and $\lambda < 0.2$. For convenience, it is reasonable to use $\phi_s = E_s/1{,}000$ and $U_s = V_s\phi_s$ to normalize the enthalpy and total energy, respectively.

Analytical model of chiral buckling

The process of deriving the analytical model for chiral buckling is extensive and involves rigorous mathematical calculations. In Supplementary Information section 'Chiral twist buckling theory', we systematically elaborate on the geometry, deformation, force, energy, and stress induced by in-plane bending, out-of-plane bending, in-rod twisting, helix and compression modes (Supplementary Notes 2 and 3). Definitions of all variables are also listed there. Here we summery the analytical theory (also in Supplementary Note 3.8), with key parameters labelled in Extended Data Fig. 1.

When a vertical compression displacement s is applied to half a chiral metacell, a variable rotation angle θ forms between the two tori. The equivalent strain is $\varepsilon = s/h_0$. The reaction force and elastic energy contributed by a single rod are F_{1rod}, U_{1rod}, respectively. Point B is fixed on torus O_1. Point A_0 is the original point on torus O_2, which moves to point A under the compression displacement s. Length is given as

$$L_s = |AB| = \sqrt{R_1^2 + R_2^2 - 2R_1R_2\cos(\theta + \alpha_0) + (h_0 - s)^2}.$$

The in-plane bending deflection is denoted as $2a_{in}$ and the out-of-plane bending deflection is denoted as $2a_{out}$. Specifying $\beta = \angle ABA_0$, $2a_{in} = L_s\sin\beta$, $L_x = L_s\cos\beta$. The term $2a_{out}$ is defined by length |CD| shown in Extended Data Fig. 1b.

The moments induced by in-plane bending and in-rod twisting (Supplementary Note 3) are

$$M_{in} = a_{in}b^2 E_s I, \quad T_{twist} = 2GI\theta_r/L_0.$$

Here $b = \pi/L_x$, $I = \pi r^4/4$ is the second moment of the rod, G is the shear modulus, $\theta_r = \theta\text{-}\gamma$. The bulge-out angle γ arises from the helical deformation of rod, as shown in Extended Data Fig. 1c.

The components of the two moments in three-dimensional spaces are

$$(M_{\text{in},x}, M_{\text{in},y}, M_{\text{in},z}) = M_{\text{in}}\boldsymbol{n}_{\text{in}},$$

$$(T_{\text{twist},x}, T_{\text{twist},y}, T_{\text{twist},z}) = T_{\text{twist}}\boldsymbol{n}_{\text{twist}}.$$

where $\boldsymbol{n}_{\text{in}}$ is the unit normal vector of the in-plane bending and $\boldsymbol{n}_{\text{twist}}$ is the unit normal vector in the twisting deformation. The concentrated force applied on a single rod denotes (F_x, F_y, F_z). We use the following equations to analyse chiral buckling deformation and calculate energy.

1. Force equilibrium equation (Supplementary Fig. 7)

$$\begin{cases} 2M_{\text{in},y} - F_x(h_0 - s) - F_z(R_1 - R_2\cos\alpha) = 0, \\ 2M_{\text{in},z} + F_xR_2\sin\alpha + F_y(R_1 - R_2\cos\alpha) = 0, \\ M_{\text{in},z} + T_{\text{twist},z} + F_xR_2\sin\alpha - F_yR_2\cos\alpha = 0. \end{cases}$$

Here $\alpha = \theta + \alpha_0$. Based on this equation, the compressive load applied on a chiral rod is $F_{1\text{rod}} = -F_z$.

2. Compatibility equation of deformation

$$L_{\text{in}} = L_0 - \eta\Delta_{\text{out}} - \Delta_{\text{cpr}},$$

where $\Delta_{\text{out}} = \pi^4 a_{\text{out}}^2/4L_s$ denotes the shortening made by out-of-plane deformation; Δ_{cpr} is the pure compression displacement along the rod, and $\Delta_{\text{cpr}} < \pi r^2/L_0$; $L_{\text{in}} = \frac{E_k(\pi, -a_{\text{in}}^2 b^2)}{b}$ denotes the length of the rod under in-plane deformation, and $E_k(\cdot)$ is the elliptical equation; η denotes a correction factor explained in Supplementary Note 3.4.

3. Energy equation

$$U_{1\text{rod}} = \frac{E_sI\pi^4 a_{\text{in}}^2}{4L_x^3} + \frac{E_sI\pi^4 a_{\text{out}}^2}{L_0^3} + \frac{GI_p\theta^2}{2L_0} + \frac{K_c\Delta_{\text{cpr}}^2}{2}.$$

Here $K_c = E_s\pi r^2/L_0$ denotes the longitudinal stiffness of the rod. Based on the energy method, the compressive load is

$$F_{1\text{rod}} = \frac{\partial U_{1\text{rod}}}{\partial s}.$$

4. Equation of stresses

The maximal stresses induced by in-plane bending, in-rod compression and twisting are

$$\sigma_{\text{in}} = \frac{E_s r\pi^2 a_{\text{in}}}{L_s^2}, \quad \sigma_{\text{cpr}} = \frac{F_{1\text{rod}}}{\pi r^2}, \quad \tau = \frac{G\theta_r r}{L_0}.$$

Here σ_{in} and σ_{cpr} are in the same direction, $\sigma_{\text{norm}} = \sigma_{\text{in}} + \sigma_{\text{cpr}}$. At the same point, the direction of twisting shear stress τ is perpendicular to σ_{norm}. The stress in the radial direction of the rod is negligible. According to the theory of equivalent von Mises stress,

$$\sigma_v = \sqrt{\sigma_{\text{norm}}^2 + 3\tau^2}.$$

We adopt this equivalent stress to evaluate the strength of the rods in the chiral structure.

Stress evaluation

The shear modulus is $G = E_s/2(1+\upsilon)$, where Poisson's ratio is $\upsilon = 0.3$. In the chiral metacell, both the in-plane and out-of-plane bending deflection follow the function $1 - \cos(\pi x/L)$, with their deflection amplitudes denoted as $2a_{\text{in}}$ and $2a_{\text{out}}$, respectively. In-rod twisting generates shear stress given by $\tau = E_s\pi r/2.6L_0 = \sigma_{\text{bend}}(L_0 - s)^2/2.6L_0\pi a$. A proper chiral structure sets $L_0 \approx 4R$; under large deformation, $s \approx R$ and the in-plane bending deflection $2a \approx 2R$. Thus, we find that $\tau \approx 0.3\sigma_{\text{bend}}$. Under the same compressive displacement s, σ_{norm} in the chiral rod and the lattice rod (Fig. 1a) are approximately equal.

Performance evaluation

We use the following quantities to evaluate the performance.

$$\text{Equivalent strain } \varepsilon = s/h_0,$$
$$\text{Enthalpy } \phi = U_{\text{cell}}/V_{\text{cell}},$$
$$\text{Equivalent stress } \sigma_{\text{eq}} = F_{\text{cell}}/A_{\text{cell}},$$
$$\text{Mass density } \rho = m_{\text{cell}}/V_{\text{cell}}.$$

Here, force F, energy U, volume V, mass m, the projected area in load-bearing direction A and the vertical compression displacement s, with the subscript 'cell' are measured on the unit cell. The equivalent elastic modulus E denotes the slope of the ε–σ_{eq} curve at a small strain $\varepsilon < 0.02$. The maximal stress on the buckling plateau, $\sigma_{\text{bk}} = \max(\sigma_{\text{eq}})$, symbolizes the load-bearing strength of the entire metamaterial. These variables are normalized for evaluation as E/E_s, σ_{bk}/E_s, ϕ/ϕ_s and ρ/ρ_s, where ρ_s is the mass density of the rod material, $\phi_s = E_s/1{,}000$ is defined in the section 'Parameter generalization'.

For a chiral metamaterial, there are N rods around the circle with radius R. Here we adopt the integral $N = \text{Round}(\pi R/2r)$ with enough space left to avoid contact between the deformed arms. Thus, $V_{\text{cell}} = 4h_0(R+r)^2$, $A_{\text{cell}} = 4(R+r)^2$, $F_{\text{cell}} = NF_{1\text{rod}}$, $U_{\text{cell}} = NU_{1\text{rod}}$, $m_{\text{cell}} = Nm_{\text{rod}}$, where m_{rod} is the mass of a rod. Here we adopt the maximal cubic volume and square area, instead of the smaller cylinder and circular sizes, to evaluate the performance of chiral metamaterials.

For octahedron lattices, we calculate only 1/8 metacell corresponding to one rod. The parameters are defined as follows: $F_{\text{cell}} = F_{1\text{rod}}$, $U_{\text{cell}} = U_{1\text{rod}}$, $m_{\text{cell}} = m_{\text{rod}}$, $V_{\text{cell}} = (L_{0r}^3\cos^2\theta\sin\theta)/2$, $A_{\text{cell}} = (L_{0r}^2\cos^2\theta)/2$ where θ denotes the oblique angle between the rod and the horizontal. L_{0r} denotes the distance between the neighbour connection nodes.

For prism lattices, we calculate only 1/4 metacell corresponding to one rod. $F_{\text{cell}} = F_{1\text{rod}}$, $U_{\text{cell}} = U_{1\text{rod}}$, $m_{\text{cell}} = m_{\text{rod}}$, $V_{\text{cell}} = l_pL_{0r}^2\cos^2\theta\sin\theta$, $A_{\text{cell}} = l_pL_{0r}\cos\theta$, where l_p denotes the distance between neighbouring rhombuses, that is, the lattice constant along the x-axis in Fig. 4. Here we adopt $l_p = 4r$ to form a dense lattice.

For octahedron and prism lattices, the useful length of a rod is L_0. In the above equations, L_{0r} denotes the distance between two connection nodes in lattices. If $L_{0r} = L_0$, we will obtain $\rho/\rho_s > 1$, when the oblique angle $\theta > 70°$, which is impractical. In reality, the connection nodes also occupy space, as shown by the samples in Fig. 4. Therefore, the practical lattices have $L_{0r} > L_0$. For our calculations, we adopt a reasonable value $L_{0r} = 1.1L_0$ for the rod with $r = 1.5$ mm.

Samples

The rubber chiral metacell in Fig. 4a features $N = 8$ rods with $r = 1.5$ mm, whereas the titanium version has $N = 20$ and $r = 0.6$ mm. All samples have $h_0 = 30$ mm or $L_0 = 30$ mm. Both the rubber and titanium chiral samples in Fig. 4a,b have $R = 7.5$ mm and $\alpha_0 = 5°$. The oblique angle in prism lattices is $\theta = 40°$. The distance between the neighbour parallel rods is 3 mm for the TC4 lattice and 10 mm for the rubber lattice. The rods inside octahedron and tetradecahedron lattices have equal length. Based on Fig. 3, the in-rod maximal Mises stresses in chiral, prism and octahedron lattices are approximate when the same global strain ε is specified. Although tetradecahedron and tensegrity lattices can theoretically endure higher global deformation, their neighbouring rods make contact when $\varepsilon > 0.4$. Our performance evaluation takes these differences into account. Other parameters and results are listed in Extended Data Table 1.

In Fig. 4c, chiral-20° has $R = 5.5$, $2r = 1.8$, $\alpha_0 = 20°$, $h_0 = 20$ mm. Chiral-50° has $R = 6$, $2r = 1.7$, $\alpha_0 = 50°$, $h_0 = 20$ mm. $E_s \approx 5.5$ MPa for rubber samples in Fig. 4e, whereas other rubber samples have $E_s \approx 15$ MPa.

Experiments

Cyclic compression experiments were performed. The rods in newly fabricated metal samples are initially straight. However, after the first compressive cycle, the all-metal samples exhibit some residual plastic deformation. In this case, α_0 increases, and the rod becomes slightly bent. Moreover, the first cycle strengthens the material, improving its overall strength. Subsequent compression cycles are fully repeatable, that is, no further plastic deformation occurs. The enthalpy is calculated as $\phi = \int \sigma_{eq} d\varepsilon$.

For the prism lattice, the one-layer sample shown in Extended Data Fig. 9a consists of two half metacells. We tested the deformation of two-layer and four-layer samples to confirm consistency. For multilayer prism lattices, out-of-plane bulge-out deformation (corresponding to 1/2-order buckling) occurs when there are no lateral constraints (see Extended Data Fig. 9b and Supplementary Video 5). This deformation reduces the buckling strength σ_{bk} and enthalpy ϕ by a factor of 10 compared with the desired in-plane buckling mode shown in Fig. 1a (Extended Data Fig. 9h). Therefore, as shown in Extended Data Figs. 9c and 10e, we placed the prism lattices inside a box to constrain the lateral bulge-out deformation.

Data availability

The analytical models, sample parameters, simulation and test data supporting the findings of this study are available in the paper, Extended Data figures and Extended Data table, and Supplementary Notes. Further details are available from the corresponding authors upon request.

Code availability

The FEAs are performed with ANSYS software package, which is available at https://www.ansys.com. Other codes about analytical model can be programmed with equations listed in Methods and Supplementary Notes.

Acknowledgements This research was funded by the National Natural Science Foundation of China (projects numbers 52322505, 52241103 and 11991032), the Natural Science Foundation of Hunan Province (projects number 2023JJ10055). P.G. acknowledges support from the Deutsche Forschungsgemeinschaft (DFG, German Research Foundation) through the Excellence Cluster 3D Matter Made to Order (EXC-2082/1–390761711). We thank X. Liu and S. Forest for their discussions on mapping to micropolar elasticity.

Author contributions X.F. conceived the idea, established the analytical models and performed the experiments. X.F. and P.G. designed the study. X.F., P.G., H.G. and D.Y. conducted the numerical simulations and designed the experiments. J.W. designed experimental setups. Y.D. fabricated samples. Y.D., D.Y. and J.W. conceived application cases. M.R.B. and H.G. analysed the properties. All authors interpreted the results. X.F., H.G., M.R.B. and P.G. wrote the paper with input from all authors.

Competing interests The authors declare no competing interests.

Additional information
Supplementary information The online version contains supplementary material available at https://doi.org/10.1038/s41586-025-08658-z.
Correspondence and requests for materials should be addressed to Xin Fang or Peter Gumbsch.
Peer review information *Nature* thanks Muamer Kadic and the other, anonymous, reviewer(s) for their contribution to the peer review of this work. Peer reviewer reports are available.

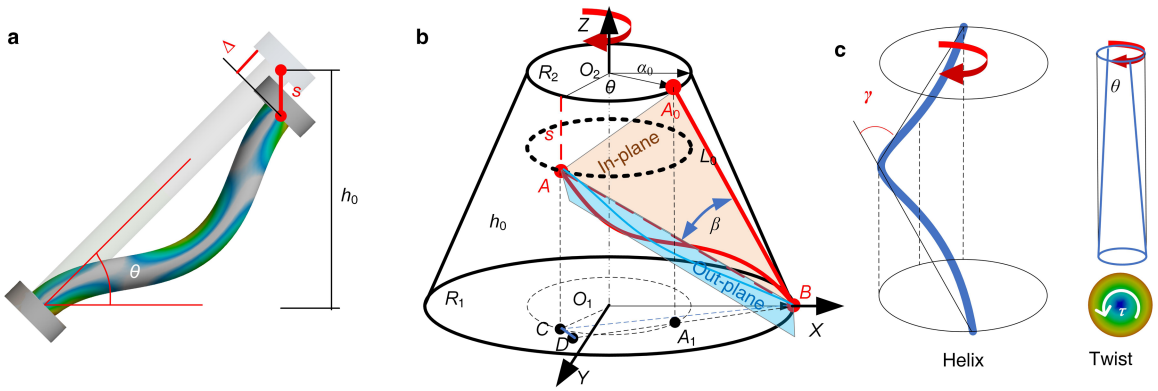

Extended Data Fig. 1 | Model description. (a) Compressive buckling of an oblique rod in a nonchiral lattice. (b) Model of half a chiral metacell (Supplementary Note 2), showing the in-plane and out-of-plane bending deformations (Supplementary Note 3.1 and 3.2). XYZ denotes the global coordinates. (c) A twisted rod becomes helical, indicating the bulge-out angle γ (Supplementary Notes 3.3 and 3.4). Taking arm A_0B as an example, point B is fixed to axis O_1X, and point A_0 is on torus O_2. The relative rotation angle at rest between the two tori is α_0. When torus O_1 is fixed, torus O_2 generates a dynamic rotation angle θ under the compressive displacement s, resulting in chiral deformation. Point A_0 moves to A, while the rod is twisted by angle θ. The subpoints of A and A_0 on plane XOY are C and A_1, respectively.

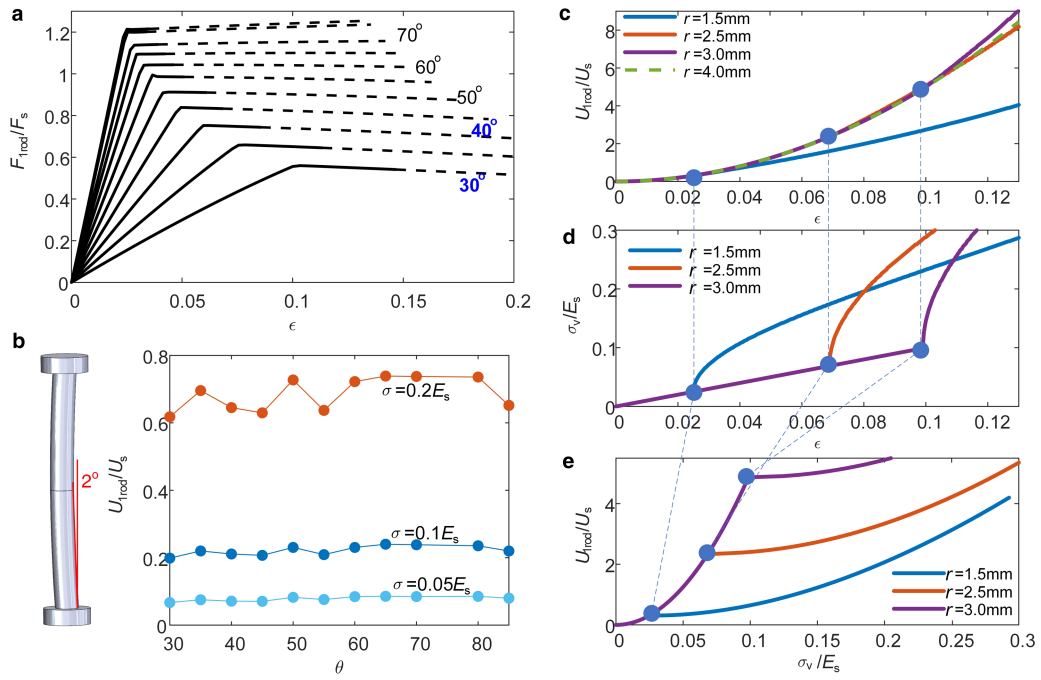

Extended Data Fig. 2 | Buckling of perfect and nonperfect straight rods. Unless otherwise labeled, $r = 1.5$, $L_0 = 30$ mm. For metamaterial consisting of oblique rods, applying a vertical compressive displacement (s) gets an equivalent strain $\varepsilon = s/h_0$. In (b, c, d), the rods are vertical. (a) Normalized compressive force of the perfectly straight rod with different oblique angle. The dashed range represents $\sigma_v > 0.1E_s$. Bending buckling happens abruptly. (b) Normalized strain energy of a micro-bending rod under different stress. The rod center is bended by 2°. This small imperfection greatly reduces the normalized energy under $\sigma_v = 0.05E_s$, $\sigma_v = 0.1E_s$ and $\sigma_v = 0.2E_s$ by about 2/3, compared to the perfectly straight rod shown in Fig. 2 in the main text, due to stress concentration at the bent position. Fortunately, comparing Fig. 2a in the main text, the maximum force of this imperfect rod nearly unchanged. (c, d) Analytical solution of energy and von Mises stress as a function of equivalent strain for a rod. (e) Energy-stress curves combined from panels (c, d). The original rod is perfectly straight. Panel (d,e) indicates the two-stage deformation process of a nonchiral straight rod. Panel (c) indicates that: (1) When buckling occurs, the normalized energy U_{1rod}/U_s increases at a higher rate as strain increases; (2) When $r < 2.5$ mm, thicker rod achieves higher U_{1rod}/U_s within moderate strain ($\varepsilon = 0.12$) because the contribution from pure compression increases. However, further increasing r cannot increase U_{1rod}/U_s because buckling no longer occurs. (3) In the pure compression stage, U_{1rod}/U_s is independent of rod thickness. As indicated by equation (1), σ_{cpr} gets 8 times higher increment ratio than σ_{bend} when increasing stress. Thus, for a specified moderate stress, like $\sigma_v = 0.1E_s$, a thicker rod obtains higher U_{1rod}/U_s until buckling disappears at this stress level. If the material strength limit is relaxed, hybrid bending and axial shortening will always result in higher energy storage within the specified material volume.

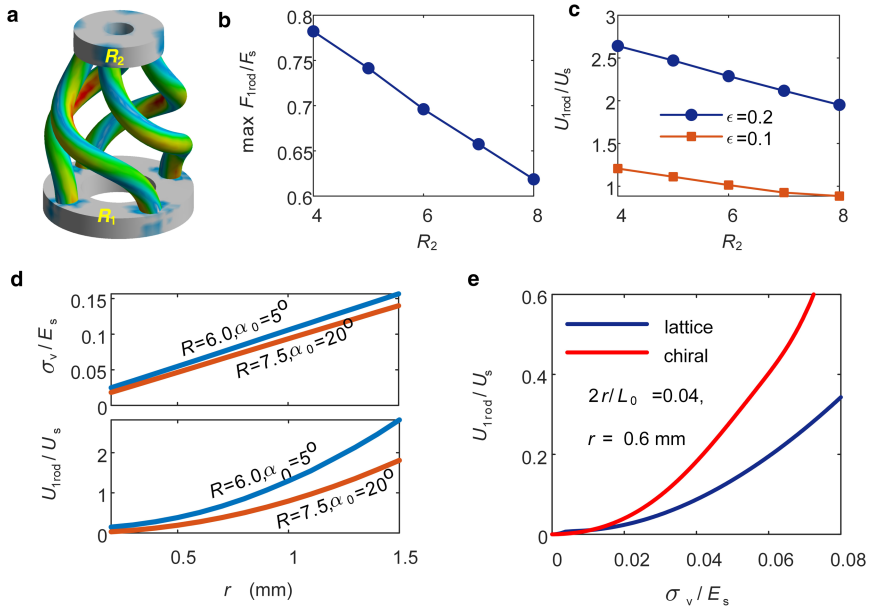

Extended Data Fig. 3 | Deformation and influences of parameters. (a) Deformation of a chiral metacell with $R_1 > R_2$. (b, c) Influence of radius R_2 on the maximum force max(F_{1rod}) and energy of the chiral rod for $R_1 = 8$ mm and $\alpha_0 = 10°$. (d) Influences of rod radius r on the stress and energy of a chiral rod at a specified strain $\varepsilon = 0.2$. (e) Energy-stress plot of a thinner rod with $r = 0.6$ mm. For all plots, $L_0 \approx h_0 = 30$ mm, and $r = 1.5$ mm for (a-d).

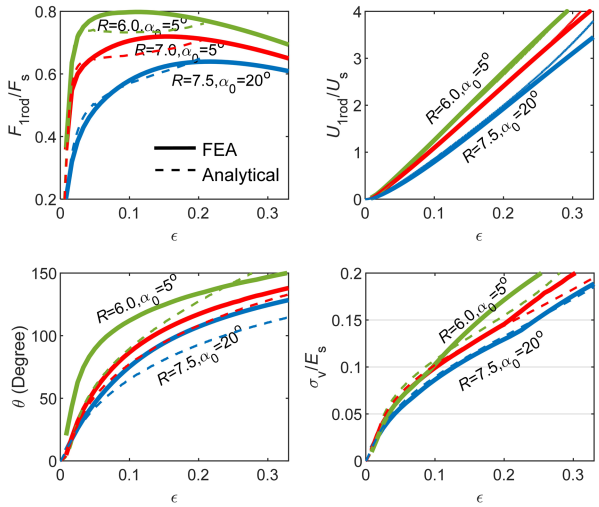

Extended Data Fig. 4 | Analytical and FEA results of typical chiral models. The four panels show the generalized force F_{1rod}/F_s, generalized energy U_{1rod}/U_s, twisting rotation angle of the chiral unit θ, and generalized stress in rod σ_v/E_s versus global equivalent strain $\varepsilon = s/h_0$. All panels share the same legends as panel 1. In these models, $R_1 = R_2$, $r = 1.5$ mm.

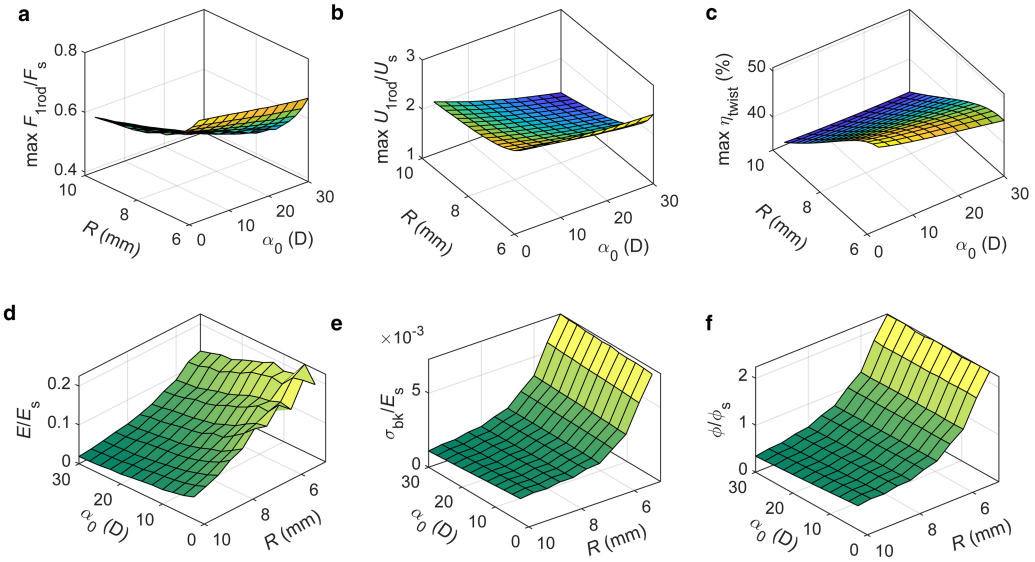

Extended Data Fig. 5 | Influences of α_0 and $R = R_1 = R_2$ on properties. (a-c) Maximum normalized force F_{1rod}/F_s, normalized energy U_{1rod}/U_s, and proportion of twisting energy η_{twist} under specified strain $\varepsilon = 0.2$. (d-f) Normalized elastic modulus E/E_s, buckling strength σ_{bk}/E_s, (c) enthalpy ϕ/ϕ_s of chiral metamaterials under specified equivalent strain $\varepsilon = 0.2$.

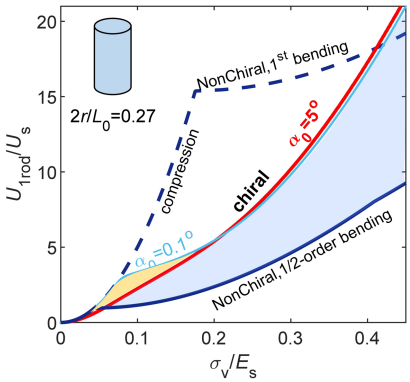

Extended Data Fig. 6 | Stress-energy curves for very thick rod. The rod has $2r/L_0 = 0.27$, $L_0 = 30$ mm. Thick rods may favor nonchiral designs in moderate stress ranges, assuming the 1st bending mode remains dominant. However, in practice, thick rods without the assistance of rigid constraints often follow a 1/2-order lateral buckling mode because its critical buckling energy is only 1/16 of the 1st mode (Methods). In this case, chiral rod still offers 2–4 times higher energy storage. Moreover, reducing the initial angle α_0 to 0.1° can improve chiral rod's performance near the critical point. The influences of α_0, R, and the rod thickness-length ratio $2r/L_0$ highlight the importance of design in chiral metamaterials.

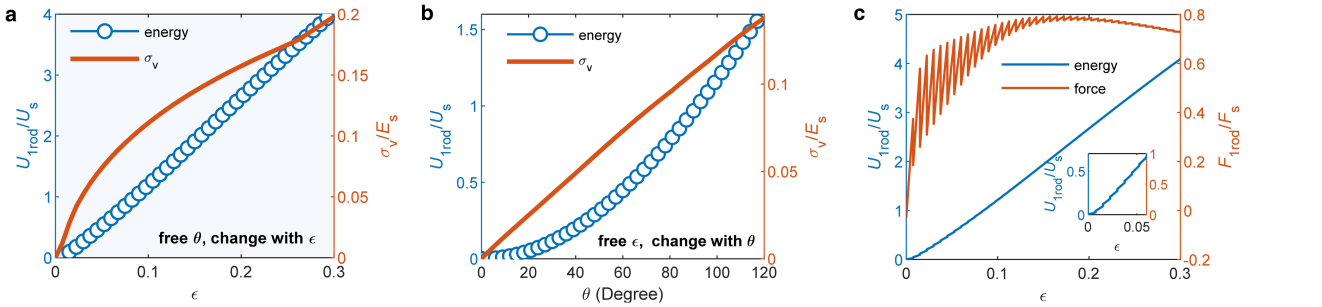

Extended Data Fig. 7 | FEA results showing the contribution of in-rod twisting and global torsion. FEA simulations are performed using the same chiral model under different boundary conditions. $R = 7, r = 1.5, h_0 = 30$ mm; $\alpha_0 = 5°$. (a) Compressive-twisting buckling: rotation θ is free for a specified compression ε. This is the boundary condition used in the main text to generate compressive chiral buckling. (b) Purely twisting condition without external compression: θ is specified, with free ε. Results from this condition indicate the contribution from in-rod twisting. In this case, all energy is contributed by global torsion because the global compressive force is zero for freely compressive boundary. Comparing U_{1rod} in (a) and (b), we obtain the energy ratio of in-rod twisting is $\eta_{twist} = 1.6/4 = 40\%$ at $\theta = 120°$, matching the analytical result in Fig. 2d. (c) Results for step simulation used to separate global torsion and global compression. From n to $n+1$ step ($\varepsilon_{n+1} = \varepsilon_n, \theta_{n+1} = \theta_n + \Delta\theta$); from $n+1$ to $n+2$ step ($\varepsilon_{n+2} = \varepsilon_{n+1} + \Delta\varepsilon, \theta_{n+2} = \theta_{n+1}$). Separating the total energy accumulated by global compression or torsion steps shows that the contribution from global compression can reach 95 - 100%. This is correct because the freely rotatable boundary condition under specified compression induces zero global torque, and thus the work done by global torque is zero. The nonlinear micropolar model in the Supplementary Note 4 indicates that all energy is contributed by chirality, as "chirality" is defined as the coupled axial force (global compression force) generated by global torsion in the micropolar model.

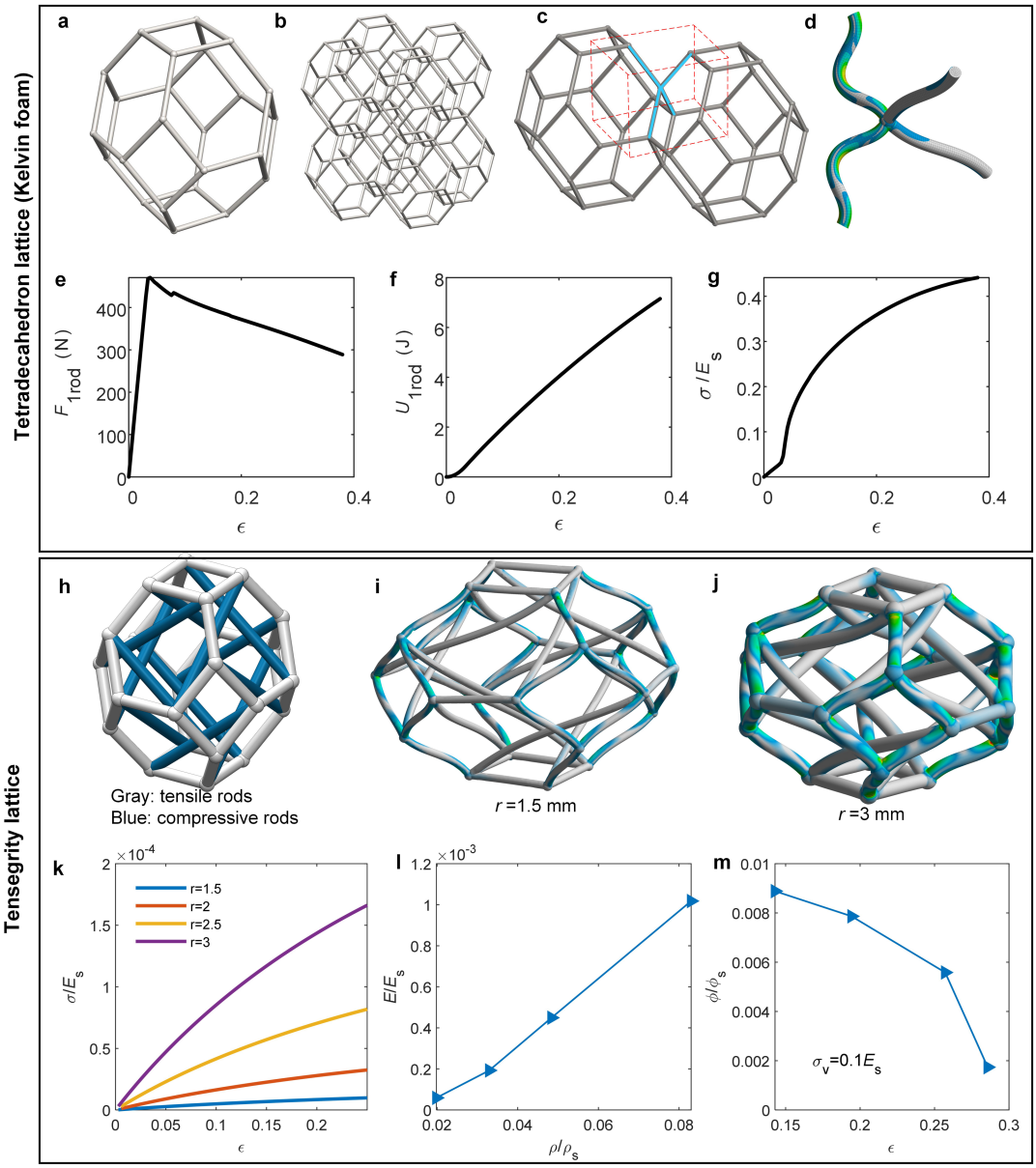

Extended Data Fig. 8 | Properties of tetradecahedron and tensegrity lattice. (a-g) Tetradecahedron (Kelvin) lattice. (h-m) Tensegrity tetradecahedron lattice. (a, h) A metacell. (c,d) Rods in 1/8 model and corresponding compression bending deformation. (e, f, g) Changes in F_{1rod}, U_{1rod} and generalized stress σ_v/E_s with equivalent strain ε. In Kelvin lattice, every rod is same with $r = 1.5$, $L_0 = 30$ mm. The size of the round connection nodes is considered. The Kelvin lattice has: $\rho/\rho_s = 7.78\times10^{-3}$, $E/E_s = 1.7\times10^{-3}$, $\sigma_{bk}/E_s = 5.7\times10^{-5}$, $\phi/\phi_s = 3.07\times10^{-3}$ at $\sigma_v = 0.2E_s$. Its buckling strength σ_{bk}/E_s is 1/5 and its enthalpy is 1/19 of the octahedron lattice with rod's oblique angle near 40°. Thus, its enthalpy is lower than 1/100 of the chiral metamaterial. In (h-m), we calculate the nonlinear compressive responses of a tensegrity metacell. All tensile and compressive rods in metacell have same radius, and ρ/ρ_s is varied by changing the rod radius. The stress σ_v is picked near the rod's end instead the rods' crossing positions where stress concentration occur. At $\sigma_v = 0.1E_s$. Enthalpy ϕ/ϕ_s for $r = 3$ mm is 5 times of the case with $r = 1.5$ mm. However, even for the tensegrity metacell with $r = 3$ mm, its enthalpy is only 1/4 of the same-density octahedron lattice consisting of rod with $r = 1.5$ mm.

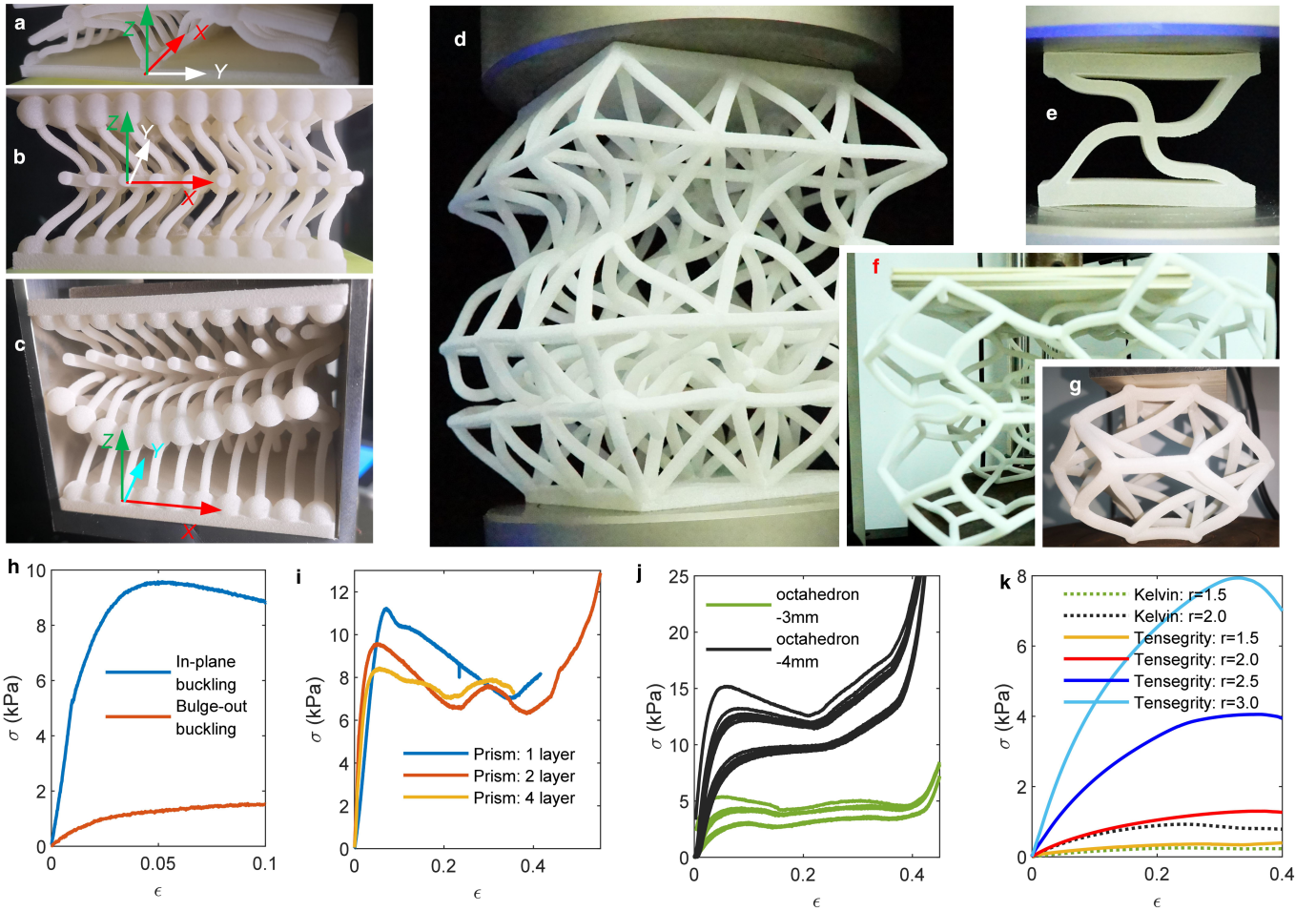

Extended Data Fig. 9 | Experimental results of nonchiral rubber lattices. (a) Buckling of a single-layer rubber prism lattice. (b) Bulge-out buckling of a two-layer rubber lattice without rigid constrains, with the center bugle-out along the x-axis. The view in (a) is different from (b,c). (c) In-plane buckling of a four-layer rubber lattice placed inside a box. (d) Compression buckling of the octahedron lattice. (e) Deformation of the plate-based prism lattice. (f) Deformation of the tetradecahedron (Kelvin) lattice. (g) Deformation of the tensegrity tetradecahedron lattice. (h) In-plane and bulge-out buckling curves of the two-layer rubber prism lattice. (i) Equivalent strain-stress curves of rubber prism lattices with one, two or four layers, where only in-plane buckling occurs. The result for the two-layer sample is shown in Fig. 4 of the main text. This panel confirms the consistency of the performance of prism lattices across different layers. (j) Equivalent strain-stress curves of octahedron lattices consisting of rods with radii $r = 1.5$ and 2 mm. (k) Equivalent strain-stress curves of the Kelvin lattices and tensegrity lattices consisting of rods with different radii. Experimental processes are shown in the Supplementary Videos. **Notes:** In performance evaluations and comparisons, every rod in these nonchiral lattices is assumed to have ideal 1st-order bending deformation. For the prism lattice, this is achieved by constraining lateral deformation. However, in experiments, different layers in octahedron lattices do not buckle simultaneously due to intrinsic instability [*Programmable Materials* 1, 1–18 (2023)], and it is difficult to induce the desired bending mode in the tetradecahedron rods. As a result, the experimental performance of multi-layered octahedron and tetradecahedron lattices may be lower than theoretical predictions.

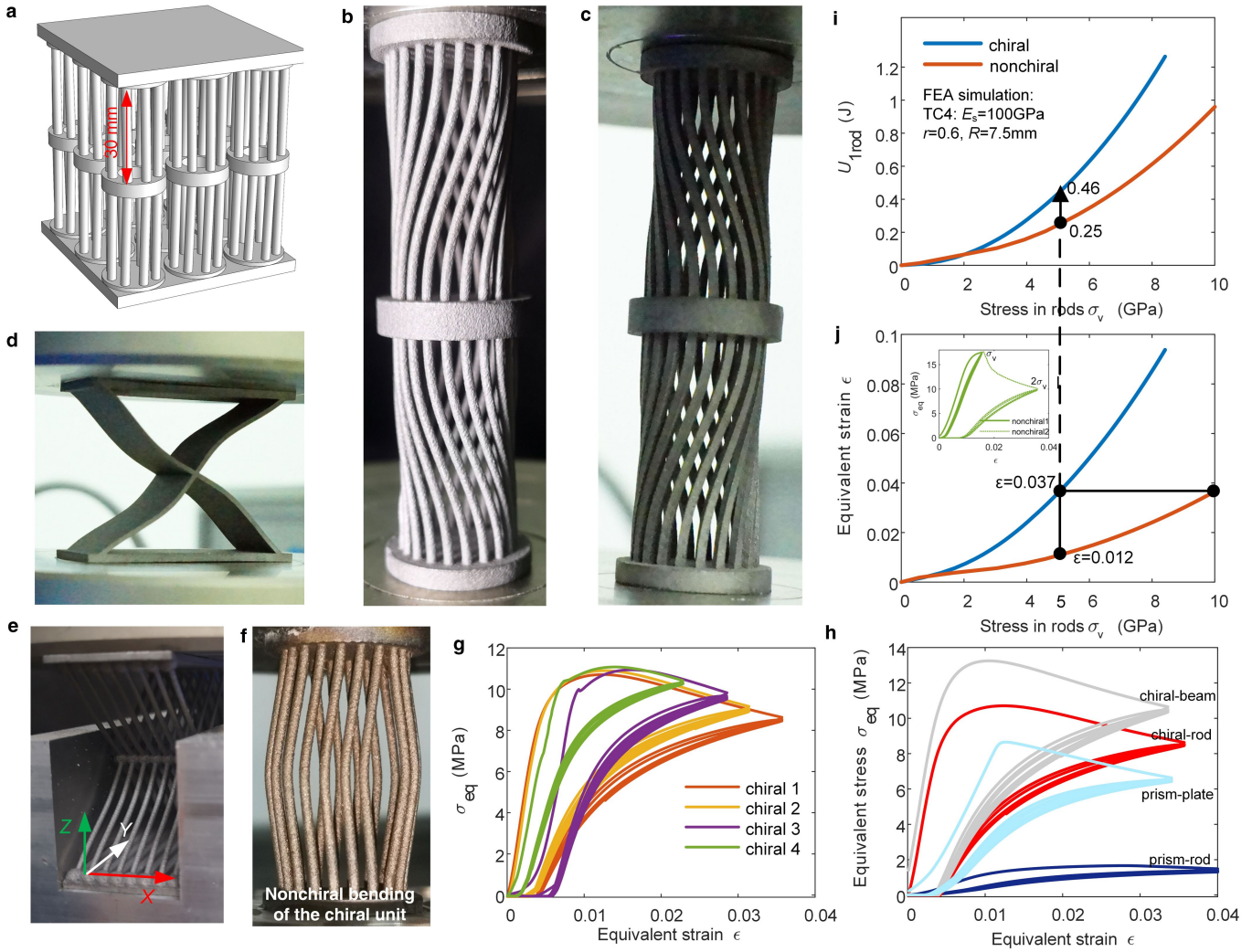

Extended Data Fig. 10 | Experimental results of chiral and nonchiral metamaterials. (a-f) Deformation images under compression for different metamaterials. (a) 3D model of the 3 × 3 rubber chiral metamaterial. Samples in (b-f) are made of TC4 titanium-alloy. (b,c) Deformation of rod- and beam-based chiral units. (d, e) Plate- and rod-based prism lattices. (f) Identical chiral unit under non-rotatable boundary conditions, presenting nonchiral bending rods. (g) Equivalent strain-stress curves of titanium alloy chiral metacells. There are four samples shown, with "chiral 2" used in Fig. 4 of the main text. (h) Equivalent strain-stress curves of different titanium alloy metamaterials. (i, j) FEA results for the identical TC4 chiral unit. "Chiral" and "nonchiral" refer to rotatable and non-rotatable boundary boundary, respectively. At the equivalent strain ε = 0.037, the real maximum Mises stress in the rod max(σ_v) is about 5 GPa for the chiral unit, but around 10 GPa for the nonchiral rod. For nonchiral deformation, ε = 0.012 for max(σ_v) ≈ 5 GPa. For a specified stress of max(σ_v) ≈ 5 GPa, the energy stored by chiral deformation is 1.84 times that of nonchiral deformation. This property is demonstrated by the experimental green curves inserted in (j), where "nonchiral1" and "nonchiral2" denote the two cases with maximal stresses of σ_v ≈ 5 GPa and 10 GPa, respectively.

Extended Data Table 1 | Collection of experimental samples and results

No	Primary material	Metamaterial type	Metamaterial primitive	sample size (mm^3)	Density $\rho(kg/m^3)$	Nbk	*repeatable loading*			initial loading			Notes
							Energy (J)	*Enthalpy ϕ (kJ/m^3)*	*Energy ratio E_m* (J/g)	*Energy (J)*	*Enthalpy ϕ (kJ/m^3)*	*Energy ratio E_m* (J/g)	
1	Rubber: ρ_s=1000 kg/m3	Chiral	Rod, *r*=1.5mm	65*65*72	290.27	144	6.09	**20.02**	**0.201**				Energy at ε=0.25
2		Prism	Rod, *r*=1.5mm	100*130*100	222.46	160	2.39	**1.84**	**0.071**				
3		Octahedron	Rod, *r*=1.5mm	104*104*151	85.05	216	1.45	**0.89**	**0.032**				
4			Rod, *r*=2.0mm	104*104*151	111.38	216	4.56	**2.79**	**0.056**				
5		Tetradecahedron (Kelvin)	Rod, *r*=1.5mm	185*185*205	10.60	176	3.80E-04	**5.42E-5**	**1.03E-5**				
6			Rod, *r*=2.0mm	185*185*205	17.55	176	1.60E-03	**2.28E-4**	**2.41E-5**				
7		*Prism*	*Plate,t=3.2 mm*	*20*52*44*	*517.92*	*4*	*0.48*	***10.56***	***0.063***				
8		Tensegrity tetradecahedron lattice	Rod, *r*=1.5mm	94*94*110	18.11	48	0.112	**0.12**	**0.0064**				Energy at ε=0.4
9			Rod, *r*=2.0mm	94*94*110	32.20	48	0.363	**0.37**	**0.0116**				
10			Rod, *r*=2.5mm	94*94*110	49.28	48	1.163	**1.20**	**0.0243**				
11			Rod, *r*=3.0mm	94*94*110	70.37	48	2.232	**2.30**	**0.0326**				
12	TC4: ρ_s=4500 kg/m3	Chiral	Rod, *r*=0.6mm	20*20*64	593.75	40	5.17	**201.97**	**0.85**	8.19	319.92	1.34	σ_v≈5GPa at ε=0.036. See FEA results in Extended Fig. 10(i,j)
13		Chiral	Beam, *b*=*t*=1.2mm	20*20*64	621.09	40	5.60	**218.89**	**0.72**	9.60	375.18	1.24	
14		Prism	Rod, *r*=0.6mm	25*105*45	456.30	64	4.77	**40.38**	**0.49**	6.69	56.61	0.68	
15		Prism	plate, *t*=1.2mm	20*52*44	718.97	4	6.40	**139.89**	**0.49**	9.65	210.79	0.74	
16		Chiral: nonchiral bending	Rod, *r*=0.6mm	20*20*32	593.75	20	1.32	**103.13**	**0.43**	1.98	154.69	0.65	σ_v≈5 GPa at ε=0.014
17					593.75	21	2.17	**169.40**	**0.71**	4.80	375.31	1.57	σ_v≈10GPa at ε=0.036

Nbk denotes the number of buckled elements in the tested sample. ρ denotes the equivalent density of the whole sample including all buckled and non-buckled parts.